International Journal of Advanced Research in Engineering Technology & Science
ISSN: 2349-2819
Impact Factor: 7.10
(Peer-Reviewed, Open Access, Fully Refereed International Journal)
Email: editor@ijarets.org Volume-12 Issue-7 July-2025 www.ijarets.org

DESIGN AND PERFORMANCE EVALUATION OF A FOUR-PORT NARROWBAND MIMO ANTENNA FOR WIRELESS APPLICATIONS

Varsha Singh

Research Scholar Kalinga University Raipur Chhattisgarh

Dr. Nidhi Mishra

Kalinga University Raipur Chhattisgarh

Abstract

Wireless communication networks are expanding rapidly due to the increasing demand for internet connectivity that is both swift and dependable. As a result, it has become more vital to have antenna systems that function well. The design of a four-port narrowband multiple-input multiple-output (MIMO) antenna and the extent to which it functions well for contemporary wireless applications are shown in this study. The recommended antenna is compact, has adequate separation, and utilises the bandwidth more efficiently while operating effectively within the narrowband frequency range that was specified. In-depth simulations and performance evaluations have shown that the antenna exhibits improved data flow, reduced mutual coupling, and dependable connection quality. This quality makes it an excellent candidate for use in wireless networks of the future. According to the findings of the research, the proposed four-port NB-MIMO antenna has the potential to be of use in providing service to the Internet of Things (IoT), smart city networks, and emerging communication technologies such as 4G/LTE and 5G.

Keywords: Narrowband Antenna, MIMO, Four-Port Antenna, Wireless Communication, Spectrum Efficiency, Data Throughput, Mutual Coupling, Smart Cities, IoT, 4G/LTE, 5G

Introduction

The wireless communication technologies change so fast, tiny, efficient, and effective antenna systems are in high demand. In multipath fading and interference-prone environments, antennas for the Internet of Things (IoT), smart cities, and next-generation mobile networks must deliver reliable connections, quick data transmission, and superior frequency economy. MIMO antenna systems provide greater signal variation, less mutual coupling, and better channel capacity, making them a suitable solution. Narrowband (NB) antennas operate better in particular frequency bands, making them crucial. This ensures 4G/LTE, Wi-Fi, and early 5G installations are reliable and efficient. This research creates and tests a four-port NB-MIMO antenna to determine its size, compatibility with existing antennas, and suitability for future wireless communication systems. The proposed antenna design is examined for return loss, separation, radiation characteristics, and efficiency to ensure future communication network compatibility.

Narrowband antennas, also known as NB antennas, are often used in Internet of Things (IoT) nodes nowadays because of their ease of use and energy economy. On the other hand, these antennas have several drawbacks, such as a limited signal strength and a lack of directionality, which may be detrimental to the overall performance of Internet of Things networks. This is especially true in settings that need a high level of dependability and extensive coverage. Development of Narrowband Multiple Input Multiple Output (NB MIMO) antennas is gaining pace as a feasible option for Internet of Things applications. This is being done in order to overcome the issues that have been presented.

This Study presents a unique design for a four-port NB MIMO antenna, which is accomplished via a two-stage development procedure. The design in question is presented in this Study. During the first stage, the primary emphasis is on the development of a narrowband antenna that is both small and capable of functioning effectively within the sub-6 micro-GHz frequency range. Modern wireless communication systems, such as 5G, rely on this frequency spectrum because it optimizes both propagation characteristics and data delivery capacity. The antenna's compact size makes it ideal for space-constrained Internet of Things nodes, even though the design prioritizes consistent emission patterns and strong gain performance.

The creation of a four-port quad-band Double-Sided MIMO (DSMIMO) antenna arrangement is the focus of the second stage of the process. Through the use of this architecture, several frequency bands are supported, which enables simultaneous data transmission and reception across a variety of wireless protocols. Because of the double-sided construction, the isolation between antenna components is improved, which in turn reduces the amount of mutual coupling and improves the overall performance of the system. The antenna is also capable of catering to a broad variety of Internet of Things applications that work across a variety of legal and unlicensed bands thanks to its quad-band capabilities. The DSMIMO antenna that has been developed has been optimized for characteristics such as return loss, isolation, envelope correlation coefficient (ECC), and diversity gain. As a result, it is a good candidate for integration in the next generation of Internet of Things communication nodes.

Objective

1. To assess multiband MIMO antennas might reduce interference and improve network dependability in densely populated urban environments.
2. To incorporate and evaluate the developed antenna into actual smart city infrastructure, such as public safety applications, environmental monitoring, and smart traffic systems.

Compact Nb Antenna Design to Cover the Sub-6 Ghz Frequency

In the endeavour to provide robust and efficient Internet of Things connection in smart city contexts, the design and optimisation of tiny narrow-band (NB) antennas that operate within the sub-6 GHz spectrum has become an increasingly significant aspect of the effort. This section presents a miniaturised monopole antenna that has been customized to provide strong resonance and radiation characteristics within the sub-6 GHz frequency range. This range includes critical communication bands such as 1.8 GHz, 2.4 GHz, and 3.5 GHz, which are frequencies that are widely used in 4G, 5G NR, Wi-Fi, and other Internet of Things protocols. The antenna structure that has been provided has been carefully built to accomplish size reduction without sacrificing performance. This is done in order to meet the rising need for antenna solutions that are small, lightweight, and cost-effective in space-constrained Internet of Things nodes and sensor modules.

Antenna design

The created quad-band antenna may be seen in Figure 3.1, which represents its dimensions. Supposedly, a 50-ohm feed line connects a meander line radiator, an inverted 7-shaped radiator, and an I-shaped radiator to the front side of the substrate. The substrate's back side had an optimized tapered ground plane. A FR4 substrate (with an εr value of 4.4 and a tan δ value of 0.02) supports the 1.6 mm tall antenna that has been built. The tiny size (32 × 15 mm2) of the proposed antenna is its defining feature, and Table 3.1 displays the optimized characteristics.

Take notice that L1–L12 denotes radiator length, W1–W4 denotes radiator width, G1 and G2 denote the radiator gap, and Lg and Wg, respectively, denote the tapering ground planes of length and width. According to these specifications, the radiators' lengths are defined. Figure 3.2 (a) (e) shows the stages of evolution that were utilized to construct the proposed design for the quad band monopole antenna. The built antenna consists of a taper-shaped partial ground plane and the Lf × Wf structure, which stand for the feed line's length and width.

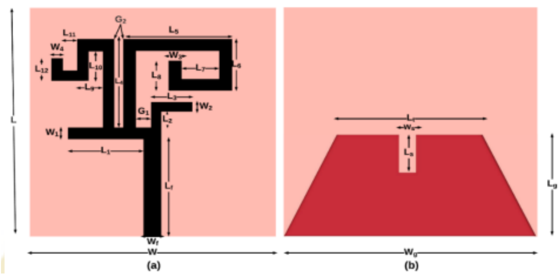

Figure 3.1. Geometry of unit cell (a) Front side (b) Back side.

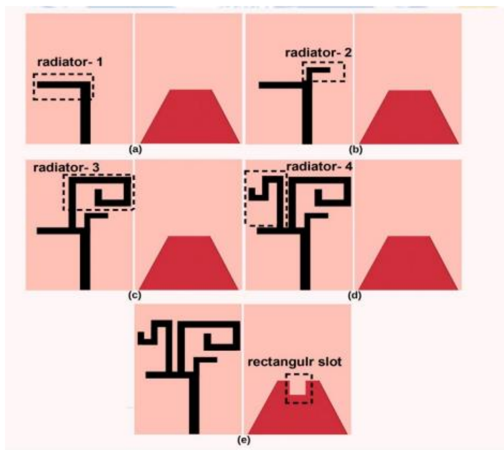

Figure 3.2. Development of proposed quad band antenna.

As illustrated in Figure 3.1, in order to guarantee that the antenna is capable of working across several bands, four distinct shaped stubs are connected to the fundamental structure. These stubs are suitably separated from one another to avoid any unwanted contact that may otherwise damage the antenna's qualities. Firstly, as shown in Figure 3.2 (a), the I-shaped stub that is quarter wavelength in length (radiator-1) is linked with the feedline that is Antenna-1. This connection forms the current route in the I-shaped stub, which can be seen from the current distribution that is shown in Figure 3.3 (a). The first resonant mode is created at 5.47 GHz as a result of the new current route. This is because the highest current is found at an I-shaped stub, as shown in Figure 3.3 (a). Equation (3.1) minus Equation (3.3) may be used to calculate the theoretical values of the first resonant mode for the I-shaped stub. The length (LS1) of the I-shaped stub plays a role in this calculation.

$$f_{ri} = \frac{C}{4L_{si}\sqrt{\varepsilon_{\text{eff}}}} \quad ; \quad i = 1, 2, 3, 4 \tag{3.1}$$

$$\varepsilon_{\text{eff}} = \frac{\varepsilon_r + 1}{2} + \frac{\varepsilon_r - 1}{2}\left(1 + \frac{12h}{w}\right)^{-1/2} \tag{3.2}$$

In this equation, the symbol 'C' represents the speed of light in a vacuum, εr represents the dielectric constant of the substrate, and Ls1 represents the overall length of the I-shaped stub antenna. According to the data shown in Figure 3.4, it is believed that the theoretical resonance frequency, which is 5.4 GHz, and the simulated resonant frequency, which is 5.47 GHz, are in considerable agreement with one another.

Table 3.1 Optimized Dimension of Quad-band Antenna

Parameters	Value (mm)	Parameters	Value (mm)
L	30	L_8	1.5
W	15	W_3	1.5
Lf	7	L_9	3
Wf	3	L_{10}	4
L_1	8.4	L_{11}	1.5
W_1	1.5	L_{12}	1.5
L_2	8.5	W_4	1.3
L_3	4.5	G_1	1.5
W_2	2	G_2	1
L_4	11	Lg	8
L_5	9	Wg	15
L_6	2.5	Ls	2
L_7	4	Ws	3

$$L_{S1} = L_1 = \frac{\lambda}{4} \approx 8.5\,\text{mm} \tag{3.3}$$

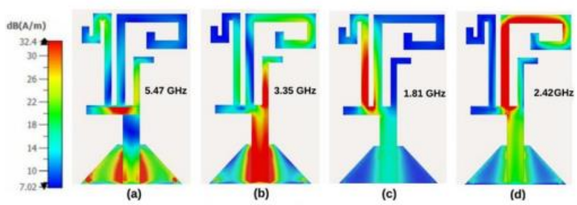

Figure 3.3. Surface Current Mapping of the Unit Cell

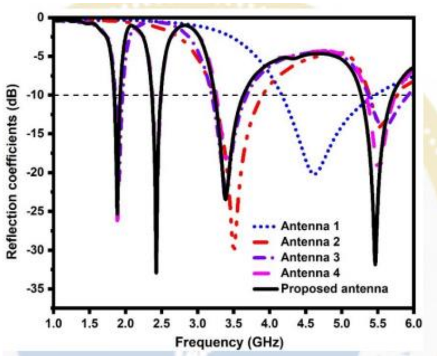

Figure 3.4. Reflection Coefficient Variation During Antenna Design Stages

As can be seen in Figure 3.2 (b), the feedline that constitutes Antenna-2 is linked to the quarter wavelength inverted L-shaped branch that is known as Radiator-2. As can be seen in Figure 3.3 (b), the current route is generated in the branch that is shaped like an inverted L. This may be seen by observing the current distribution. As a result of the revised current route, the second resonant mode manifests itself around 3.35 GHz. This is because the highest current is found at an inverted L-shaped stub, as shown in Figure 3.3 (b). It is possible to determine the theoretical values of the second resonant mode for the inverted L-shaped stub by using Equation (2.4), which is the length (LS2) of the inverted L-shaped stub.

$$L_{S_2} = L_2 + L_3 = \frac{\lambda}{4} \approx 13 \text{ mm} \tag{3.4}$$

The whole length of the L-shaped stub radiator is denoted by LS2. The theoretical resonance frequency (3.3 GHz) and the simulated resonant frequency (3.35 GHz), as shown in Figure 3.4, are quite close to one another.

Antenna-3, an I-shaped stub, is connected to Radiator-3, a stub of the quarter-wavelength meander line. Look at Figure 3.2(c) to see this link. Figure 3.3 (c) shows a current distribution example; this distribution is what generated the current route in the meander line-1 stub. As shown in Figure 3.3 (c), the third resonant mode manifests itself at 1.81 GHz as a result of the new current route. This is because the meander line-1 stub is the location where the largest current is present. It is possible to determine the theoretical values of the third resonant mode for the meander line-1 stub by using Equation (3.5), which is the length (LS3) of the meander line-1 stub.

$$L_{S_3} = L_4 + L_5 + L_6 + L_7 + L_8 = \frac{\lambda}{4} \approx 24 \text{ mm} \tag{3.5}$$

The overall length of the meander line-1 stub radiator is denoted by the symbol LS3. As shown in Figure 3.4, the theoretical and simulated resonant frequencies at 1.81 GHz are in excellent agreement with one another regarding the frequency.

Then, as indicated in Figure 3.2 (d), the quarter wavelength meander line-2 stub (radiator-4) is coupled with the above I-shaped stub that is Antenna-4, and it forms the current route in the meander line-2 stub as obvious from the current distribution as represented in Figure 3.2 (d). As shown in Figure 3.3 (d), the fact that the highest current is present at the meander line-2 stub causes the fourth resonant mode to occur at 2.42 GHz. This is because the new current route causes the maximum current to be created there. With the help of Equation (3.6), which is the length (LS4) of the meander line-2 stub, it is possible to compute the theoretical values of the fourth resonant mode for the meander line-2 stub.

$$L_{S4} = L_4 + L_9 + L_{10} + L_{11} + L_{12} = \frac{\lambda}{4} \approx 20 \text{ mm} \quad (3.6)$$

The overall length of the meander line-2 stub radiator is denoted by the equation LS4. As shown in Figure 3.4, the theoretical resonance frequency, which is 2.4 GHz, and the simulated resonant frequency, which is 2.42 GHz, are in excellent agreement with one another. I-shaped, inverted L-shaped, meander line-1, and meander line-2 stubs, as well as a tapering ground plane, are the components that make up the antenna architecture that has been built. As shown in Figure 3.2 (e), the process of design development results in the creation of a rectangular slot in the tapered ground plane. This slot is intended to increase the antenna reflection coefficient. The suggested antenna is thought to be composed of four radiators that are each a quarter of a wavelength in length. These radiators generate four resonant bands at frequencies of 1.81 (1.7–1.96) GHz, 2.42 (2.26–2.47) GHz, 3.35 (3.1–3.7) GHz, and 5.47 (5–5.65) GHz at the same time.

Parametric Analysis

In this experiment, we examine the performance of the antenna and investigate how the width of the feed and the lengths of the short grounds impact its performance.

Effect of feed line width (Wf) and defective ground length (Ls)

Figure 3.5 and Figure 3.6 display the reflection coefficient of the planned antenna for various lengths of the faulty ground plane (LS = 1, 1.5, and 2 mm) as well as for varied widths of the feed line (Wf = 1, 2, and 3 mm). The numbers are given in order of value. The broadening of the feed lines and the adjustment of the ground length have the consequence of enhancing the impedance matching within the working bands. The suggested antenna has dimensions of 2 millimeters in length and 3 millimeters in breadth. According to the parametric research, this antenna operates most effectively at 1.81 GHz, 2.4 GHz, 3.35 GHz, and 5.4 GHz waves.

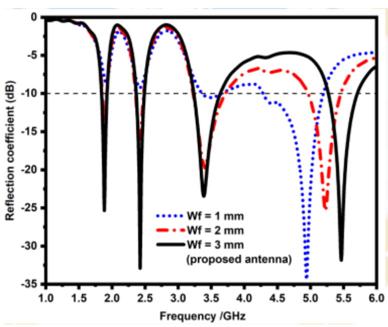

Figure 5. S11 Response of Proposed Antenna for Varying Feed Line Widths

Analogous circuit of the element that was created

Using the observed and simulated impedance values, an analogous circuit model is constructed to provide a deeper insight into the electrical behavior of the proposed multiband MIMO antenna. In order to study the antenna's resonance behavior over several frequency bands, this model provides a straightforward yet effective description of the reactive and resistive components. Results from the S-parameter study showed that the antenna's impedance curve, which shows the impedance as a function of frequency, peaks at resonant frequencies. Conversely, at a resonance point, the impedance's imaginary component often undergoes the inductive to capacitive transition, as shown by a negative slope crossing zero. A parallel RLC (Resistor-Inductor-Capacitor) circuit may imitate each resonant mode thanks to this response. Some examples of operating bands that each branch of the RLC circuit relates to include 1.8 GHz, 2.4 GHz, 3.35 GHz, and 5.4 GHz.

In order to accurately portray the multi-resonant characteristics of the antenna, the equivalent circuit is constructed by coupling numerous RLC branches in series against one another. For the purpose of imitating the bandwidth and impedance matching that was seen in the full-wave simulation, the values of R, L, and C are adjusted together. During the optimisation phase, when rapid tweaks to circuit parameters may forecast changes in antenna behaviour without the need to perform lengthy electromagnetic simulations, this comparable model serves as a significant design tool. This is particularly true during the optimisation phase. This kind of modelling is very helpful for Internet of Things (IoT) applications in smart cities, which need antenna designs that are efficient, small, and low-profile in order to function successfully across numerous wireless protocols. The equivalent circuit enables rapid prototyping and facilitates integration into a variety of Internet of Things modules. This, in turn, speeds up the deployment of high-performance MIMO-based communication systems in urban environments. This is accomplished by accurately characterising the resonant response and energy storage behaviour of the antenna structure.

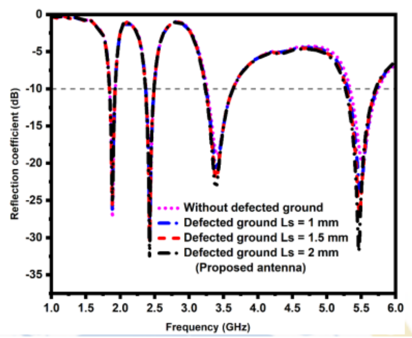

Figure 3.6. S11 Response of Proposed Antenna with Varying Ground Slot Lengths

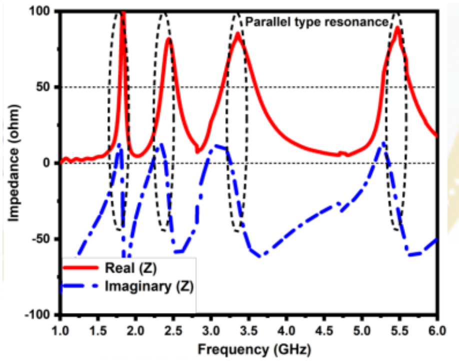

Figure 3.7. Proposed Antenna Input Impedance Characteristics

Figure 3.8 illustrates how the RLC circuit, which consists of R1, L1, and C1, correlates to the first operational band for the circuit. The second, third, and fourth RLC circuits, respectively, are the ones that are responsible for representing the operational bands 2, 3, and 4, respectively. Within the antenna equivalent circuit, the RLC values that were determined are shown in Table 3.2.

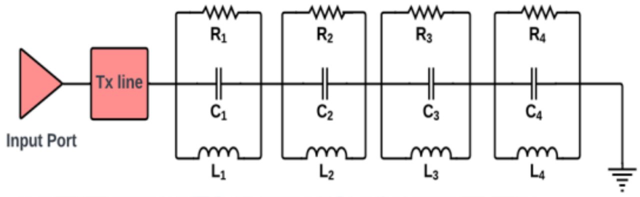

Figure 3.8. Lumped Equivalent Circuit of Proposed Antenna

Table 3.2. Parameter Values Extracted from Quad-Band Antenna

Band (GHz)	Resistance (Ω)	Inductance (nH)	Capacitance (pF)
Band 1 = 1.8	R1=1515R_1 = 1515	L1=19.3L_1 = 19.3	C1=0.403C_1 = 0.403
Band 2 = 2.4	R2=6781R_2 = 6781	L2=39.5L_2 = 39.5	C2=0.112C_2 = 0.112
Band 3 = 3.3	R3=12.67R_3 = 12.67	L3=0.11L_3 = 0.11	C3=21.34C_3 = 21.34
Band 4 = 5.4	R4=168.07R_4 = 168.07	L4=0.59L_4 = 0.59	C4=1.479C_4 = 1.479

Results and discussion

All of the significant radiation properties, including the reflection coefficient, the voltage standing wave ratio (VSWR), the radiation pattern, the gain, the overall efficiency, and the hosting effects, are covered in this section.

V.S.R. and reflection coefficients

After the production of the desired antenna on the FR4 substrate, as seen in Figure 3.9, the NA3600N network analyzer was employed to characterize the antenna. The third iteration of the proposed antenna is depicted in Figure 3.10, which also shows the measured reflection coefficient of the antenna in addition to the simulation. There are four resonance frequencies that the antenna possesses, 1.8, 2.4, 3.35, and 5.4

gigahertz, as far as anyone can tell. The comparison between the reflection coefficients and the circuit modeling accord that were observed and simulated reaches a reasonable degree of agreement. The voltage standing wave ratio (VSWR) of the antenna that was designed for the purpose of enabling additional study of the antenna is shown in Figure 3.11. The voltage standing wave ratio (VSWR) of the antenna is less than two in both the simulated and the measured data, according to the findings of the comparison of the antenna's circuit modeling at 1.8, 2.4, 3.35, and 5.4 gigahertz.

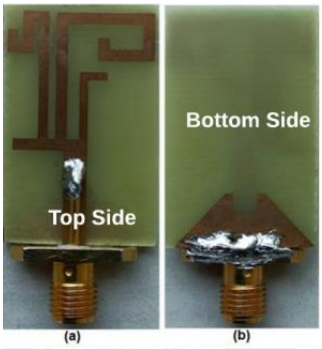

Figure 3.9. Photograph of Fabricated Quad-Band Antenna.

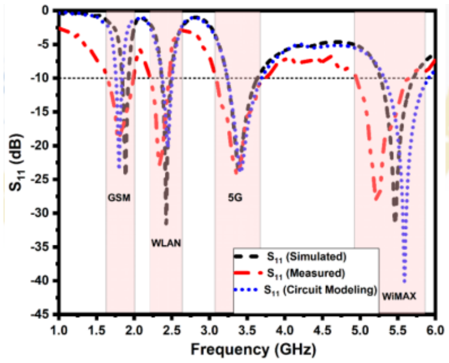

Figure 3.10. Reflection Coefficient (S11) Analysis: Simulated and Measured Results of Quad-Band Antenna.

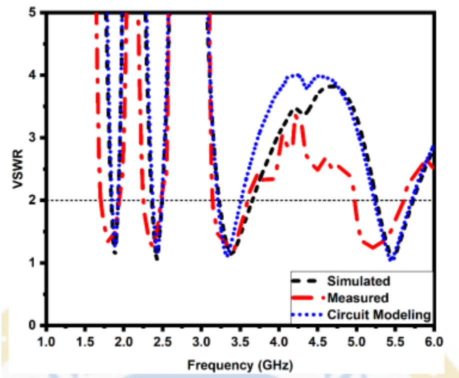

Figure 3.11. Voltage Standing Wave Ratio (VSWR) of Quad-Band Antenna.

Pattern of radiation, efficiency, and gain

In order to assess the far-field performance of the proposed multiband MIMO antenna, radiation pattern measurements are carried out in a typical anechoic chamber. This room replicates the circumstances of free space by absorbing reflections from the walls of the chamber. Due to the fact that it removes the impact of external interference and multipath effects, this environment is essential for getting precise radiation characteristics. A non-metallic positioner is used to place the antenna under test (AUT), which enables it to rotate through a full 360 degrees in both the azimuth and elevation planes. Depending on the arrangement of the test, a calibrated horn antenna is used either as the transmitting or receiving reference antenna. In order to determine the amplitude and phase of the radiated fields at a variety of angles, the chamber setup incorporates a vector network analyser, also known as a VNA.

The active microwave transmitter (AUT) is stimulated at its resonant frequencies (for example, 1.8 GHz, 2.4 GHz, 3.35 GHz, and 5.4 GHz) throughout the measurement process. The radiated power is then recorded in order to build the radiation patterns in both the E-plane and the H-plane. The patterns that were produced provide a glimpse into the directivity and symmetry of the antenna's radiation, which are essential criteria to consider when determining whether or not the antenna is suitable for omnidirectional or directional applications in smart city Internet of Things installations. In the lower bands, the DS-MIMO antenna displays radiation patterns that are steady and practically omnidirectional, which are advantageous for metropolitan coverage. In the upper bands, the antenna displays somewhat directed patterns, which are helpful in point-to-point communication situations such as smart surveillance or traffic control nodes. Due to the presence of these properties, it is evident that the suggested antenna not only offers efficient spatial coverage but also facilitates spatial multiplexing in MIMO systems, which ultimately results in an improvement in the overall reliability and performance of the network.

Figure 3.13 displays the radiation patterns of the proposed antenna at four different frequencies: 1.8, 2.4, 3.4, and 5.4 GHz. In the E and H planes, these patterns encompass both co-polarization and cross-polarization. It has been noted that in both the modeling and measurement cases, substantially omnidirectional radiation patterns were found inside the X-Z and Y-Z planes. Therefore, there is a fair amount of agreement between the radiation patterns generated by experiments and those generated by simulations.

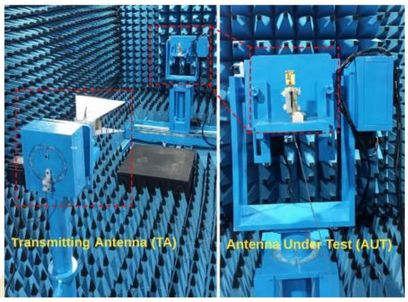

Figure 3.12. Experimental Setup for Radiation Pattern Measurement.

Efficiency analysis:

A power meter or receiver can be used to measure the amount of power that is supplied to the antenna. As measured by a voltage-node amplifier (VNA), the antenna reflection coefficient looks like this. The amount of power that the antenna could take was calculated using Equation 3.7. The E field may be measured in three distinct directions with a constant separation between them. You may use Equation 3.8 to find the total power that is released. After that, we use Equation 3.9 on the variables to find the radiation efficiency.

$$P_a = (1 - |\Gamma|^2) \cdot P_s \quad (3.7)$$

The sign Ps represents the total power that was provided to the antenna, whereas the parameter Pa represents the total power that the antenna has absorbed. By decomposing the E field into two orthogonal components, E and H, which are recorded at discrete sample sites (i, j), then Equation 3.8 may be used to determine the total radiated power. This is accomplished by decomposing the E field.

$$P_r = \frac{r^2}{120\pi} \sum_{i,j} \left(|E_\theta(i,j)|^2 + \left|E_\phi(i,j)\right|^2 \right) \sin\theta_i \Delta\theta_i \Delta\phi_j \quad (3.8)$$

$$\eta_r = \frac{P_r}{P_{tn}} = \frac{P_r}{P_r + P_l} \quad (3.9)$$

Gain analysis:

For the purpose of determining the gain based on the parameters that have been measured and the standard values, the Friis Transmission Equation 3.10 is used.

$$P_r = \frac{P_t G_t G_r \lambda^2}{(4\pi R)^2}$$

The symbol "Pr" denotes the "power at the receiving antenna," whereas the symbol "Pt" represents the "output power" of the transmitting antenna. Gt stands for the transmitting antenna gain. The receiving antenna's maximum gain is denoted by Gr, the wavelength is represented by ⅄, and the distance between the antennas is denoted by R.

The observed antenna gain and radiation efficiency are graphically shown in Figure 3.14. At a frequency of 1.8 GHz, the antenna gain was measured to be 1.5 dBi, and the overall efficiency was measured from 75%. Similar to the previous example, the gain and radiation efficiency that were tested at 2.4, 3.35, and 5.4 GHz were found to be 1.75 dBi, 2.5 dBi, and 3.7 dBi, respectively, and 78%, 80%, and 77% correspondingly.

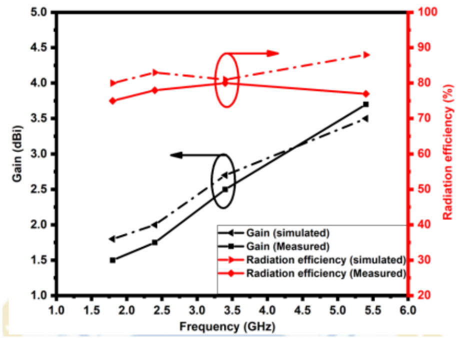

Figure 3.14. Radiation Efficiency and Gain Performance of Designed Antenna.

Conclusion

The proposed four-port narrowband MIMO antenna has been designed and tested for wireless application. It addresses the increased need for tiny, efficient, and dependable antenna systems. The investigation shows that the antenna has excellent return loss, minimal mutual coupling, and good radiation in the appropriate frequency range. Its multielement architecture improves data flow, airwave utilisation, and connection stability in multipath fading and interference environments. Integration with IoT devices, smart city infrastructures, and transportable communication systems is straightforward due to its compact size. This makes it suitable for next-generation networks. The antenna combines narrowband optimisation with MIMO to suit 4G/LTE and Wi-Fi performance requirements. It also bodes well for 5G development. Researchers may modify the design to make it reconfigurable, wideband/multiband adaptive, and real-world-tested.

References

1. Dogra, R., Rani, S., Babbar, H. and Krah, D. 2022. Energy-efficient routing protocol for next-generation application in the internet of things and wireless sensor networks. Wirel. Commun. Mob. Comput., Article ID 8006751, 1–10.

2. Faheem, M., and Gungor, VC. 2018. Energy efficient and QoS aware routing protocol for wireless sensor network-based smart grid applications in the context of industry 4.0. Appl Soft Comput, 68: 910–922.

3. Faizan, UM., Imtiaz, J. and Maqbool, KQ. 2019. Enhanced three layer hybrid clustering mechanism for energy efficient routing in IoT. Sensors, 19(4): 829.

4. Fu, X., Pace, P., Aloi, G., Yang, L. and Fortino, G. 2020. Topology optimization against cascading failures on wireless sensor networks using a memetic algorithm. Comput. Netw., 177: 107327.

5. Gao, H., Ejaz, W. and Jo, M. 2016. Cooperative wireless energy harvesting and spectrum sharing in 5G networks. IEEE Access, 4: 3647–3658.

6. Gara, F., Ben, L.S., Ben, R.A. and Tourancheau, B. 2015. RPL protocol adapted for healthcare and medical applications. In: 2015 International Wireless Communications and Mobile Computing Conference (IWCMC), 690–695.

7. Garrido-Zafra, J., Gil-de Castro, A.R., Savariego-Fernandez, R., Linan-Reyes, M., Garcia-Torres, F. and Moreno-Munoz, A. 2022. IoT cloud-based power quality extended functionality for grid-interactive appliance controllers. IEEE Trans. Ind. Appl., 58 (3): 3909–3921.

8. Gomez, C., Boix, A. and Paradells, J. 2010. Impact of LQI based routing metrics on the performance of a one-to-one routing protocol for IEEE 802.15.4 multihop networks. EURASIP J Wirel Commun Netw, 2010(1): 205407.

9. Guero, A.-M. M., Chiba, Z. and Abghour, N. 2023. Challenges and issues for Internet of Things (IoT): recent survey. Mathematical Modeling and Computing, 10(3): 796– 806.

10. Gulati, K., Sarath, R.K.B., Kapila, D., Bangare, S.L., Chandnani, N. and Saravanan, G. 2021. A review paper on wireless sensor network techniques in Internet of Things (IoT). Mater. Today: Proc., 51: 161–165.

11. Gutierrez, JA. 2003. Wireless medium access control (MAC) and physical layer (PHY) specifications for low-rate wireless personal area networks (LR-WPANs). IEEE Stand Info Technol 2003; 802(4).

12. Hassebo A. and Tealab M. 2023. Global Models of Smart Cities and Potential IoT Applications: A Review. IoT, 4: 366-411. 10.3390/iot4030017.

13. Heinzelman, WB., Chandrakasan, AP. and Balakrishnan, H. 2002. An applicationspecific protocol architecture for wireless microsensor networks. IEEE Trans. Wirel. Commun., 1, 660–670.

14. Hosen, A.S.M. S. and Cho, G. H. 2018. An Energy Centric Cluster-Based Routing Protocol for Wireless Sensor Networks. Sensors, 18(5): 1520.